

# Classifying State Uncertainty for Earth-Moon Trajectories

**Juan Gutierrez, Keric Hill**

*KBR*

**Erica Jenson, Daniel Scheeres**

*CU Boulder*

**Jill C. Bruer and Ryan D. Coder**

*AFRL/RV*

## ABSTRACT

While the evolution of state uncertainties in geocentric orbits from Gaussian to non-Gaussian is well understood, the only data product made publicly available by the United States Space Force, the Two-Line Element, does not include state uncertainties at all. With a new international focus on cislunar space domain awareness, it is necessary to determine how this complex dynamics environment influences trajectory uncertainties and the resultant implications for data association, orbit determination, and force model algorithms. This paper utilizes a new tensor eigenpair measure of nonlinearity (TEMoN) to quantify the nonlinearity of gravitational forces in the cislunar regime. This measure is then compared with various characterizations of Gaussian distributions to determine at what non-linear strength trajectory uncertainties become non-Gaussian. This novel advancement combines the cumulative effect of time and physical location of the trajectory into one value. The result is a predictive method that obviates highly parameterized Monte Carlo runs, and allows an objective assessment of how sensor tasking cadence, measurement uncertainty, and force model selection can be balanced to enable nascent cislunar space domain awareness capabilities with legacy space surveillance network assets.

## 1. INTRODUCTION

As the scientific community and commercial industry envision advanced cislunar mission concepts, this region of space between the Earth and Moon has come to the forefront of national and international interest. Cislunar traffic has already begun to increase in the last decade with the launch of the Chandrayaan-1 and Chandrayaan-2 probes, the Chang'e 5 sample return, and the CAPSTONE mission as a few examples. In order to maintain a catalogue of cislunar objects as the number of cislunar objects continues to increase, there is a need for advanced space situational awareness and space traffic management tools. Such new tools would provide improved force model algorithms, data association and orbit determination methods, and enhanced uncertainty representations to capture the full range of cislunar dynamics. While a Special Perturbations (SP) state vector and covariance can represent cislunar dynamics and Gaussian uncertainty, there is a lack of understanding of how to properly model and propagate uncertainty across the various trajectories possible within cislunar space.

This paper aims to connect the non-linear characteristics of a dynamical regime to uncertainty information, which would allow to model the uncertainty along complex trajectories and determine when it will become non-Gaussian. The quantification of nonlinearity is done with a tensor eigenpair measure of nonlinearity (TEMoN) from [11] that utilizes high-order state-transition tensors to compute TEMoN. To assess the Gaussian distribution, the Cramér-von Mises and chi-squared methods are utilized to supervise the deterioration of the distribution from a set of optimized Monte Carlo samples. A survey using TEMoN and Monte Carlo methods is used to compute a range of TEMoN values which indicate the transition of the trajectory from Gaussian to non-Gaussian. In addition, other Gaussian measures such as differential entropy and sigma-point measures are utilized along the way to observe the evolution of a Gaussian distribution. A TEMoN threshold value is chosen to predict when the uncertainty will become non-Gaussian and results from individual trajectories are compared with results from Monte Carlo methods. The trajectories are a compilation of elemental orbit families identified in [9] and a DRO family described in [20]. Initial conditions are obtained from AUTO software as implemented in [5]. The results provide an initial intuition on the link between nonlinearity and non-Gaussian uncertainty and gives insight into regions and conditions where Gaussian uncertainty breaks down. These tools and insights can be further exploited in many other algorithms.

Approved for public release; distribution is unlimited. Public Affairs release approval #AFRL-2022-4065 The views expressed are those of the authors and do not reflect the official guidance or position of the United States Government, the Department of Defense or of the United States Air Force.

## 2. TENSOR EIGENPAIR MEASURE OF NONLINEARITY

The work of presented in [11] provides a review of various Measures of Nonlinearity (MoN). The two MoN categories are deviation-based and curvature-based, and those are further divided into the local or global sub-categories. The local MoN concentrates on a single point such as the linearization point in a Taylor series expansion, where the global MoN spans the entire solution locus. The MoNs considered by Jenson and Scheeres are: the nonlinear indices in [13], the local nonlinear index from [16], and curvature measures of nonlinearity in [3]. These MoNs all require in some fashion empirical sampling or numerical optimization and many of them are heuristic. In contrast, TEMoN is semianalytical and based on tensor eigenpairs.

The TEMoN is based on the utilization of state transition tensors (STTs). The STTs are the higher-order tensors associated with a Taylor series expansion of the solution flow as in [16]. By mathematical convention, the order of a tensor is determined by the number of indices needed to define that tensor: a vector is a first-order tensor, a matrix is a second-order tensor, and so on. Therefore, the state transition matrix (STM) is a second-order tensor, and higher-order terms in the Taylor series correspond to higher-order STTs. The astrodynamics literature often refers to the STM as the “first-order STT” due to its association with the first-order derivative in the Taylor series expansion. However, the standard convention is used in this paper. Like the STM, the STTs are also computed through numerical integration. A superscript, i.e.,  $(m)$ , is used to denote the tensor order. The local dynamics tensor (LDT) can also be employed by TEMoN among other Taylor series expansions of any nonlinear model. TEMoN employs higher order STTs that contribute to the nonlinearity of the dynamics with two goals: to determine input deviations that produce the strong nonlinearity and to quantify associated degree of nonlinearity.

### 2.1 TEMoN Definition and Solution

The TEMoN definition considers a measure of nonlinearity  $\aleph_{\tilde{\Phi},m}$ , depicted by

$$\aleph_{\tilde{\Phi},m} := \max_{\delta x_0 \in X} \left| \frac{\tilde{\Phi}^{(3)} \delta x_0^3 + \tilde{\Phi}^{(4)} \delta x_0^4 + \dots + \tilde{\Phi}^{(m)} \delta x_0^m}{\tilde{\Phi}^{(2)} \delta x_0^2} \right| \quad \text{for } m > 2, \quad (1)$$

such that it is applied directly to the state-transition tensors of order  $m$ . The tensors  $\tilde{\Phi}^{(m)}$  are functions of the STTs and are computed from the squared norm of the Taylor series expansion. The term  $\tilde{\Phi}^{(2)}$  is the linear contribution to the squared norm, whereas all  $\tilde{\Phi}^{(m)}$  for  $m > 2$  include the nonlinear portion of the squared norm. The nonlinearity measure is maximized over the set of vectors  $\delta x_0$  with the magnitude  $\alpha$ ;  $\delta x_0$  is the input deviation in the Taylor series expansion. Each term in Eq.(1) is a multilinear tensor map that consists of a vector multiplied by all modes of a tensor, which produces a scalar output.

Note that the higher-order terms  $\tilde{\Phi}^{(m)} \delta x_0^m$  for  $m \geq 3$  are normalized by the linear term  $\tilde{\Phi}^{(2)} \delta x_0^2$ . This step is particularly important as it results in a comparative measure of the higher-order term to the linear term when quantifying nonlinearity. TEMoN defined as

$$\text{TEMoN}_{\Phi,m} = \max_{\delta x_0 \in X} \left| \frac{\tilde{\Phi}^{(3)} \delta x_0^3}{\tilde{\Phi}^{(2)} \delta x_0^2} \right| + \max_{\delta x_0 \in X} \left| \frac{\tilde{\Phi}^{(4)} \delta x_0^4}{\tilde{\Phi}^{(2)} \delta x_0^2} \right| + \max_{\delta x_0 \in X} \left| \frac{\tilde{\Phi}^{(m)} \delta x_0^m}{\tilde{\Phi}^{(2)} \delta x_0^2} \right|, \quad (2)$$

$$\text{TEMoN}_{\Phi,m} = \tau_3 + \tau_4 + \tau_5 \dots \tau_m, \quad (3)$$

provides a different formulation where it will produce multiple directions of nonlinearity in contrast to  $\aleph_{\tilde{\Phi},m}$ . Each direction of nonlinearity is associated with the specific order and normalized by the linear term. From Eq.(3), each order and corresponding nonlinearity direction is described by  $\tau_m$ . Given the definitions, TEMoN is an upper bound of  $\aleph_{\tilde{\Phi},m}$

$$\text{TEMoN}_{\tilde{\Phi},m} \geq \aleph_{\tilde{\Phi},m}, \quad (4)$$

where a semianalytical solution of TEMoN is found by evaluating each tensor order through a Lagrangian formulation.

The maximization of each term in Eq.(2) is based on the Lagrangian  $L_k$ , where  $k$  is the tensor order. The scalar  $\sigma$  is a Lagrange multiplier, with the constraint placed on  $\tilde{\Phi}^{(2)} \delta x_0^2$  such that it will ensure the magnitude of deviation,  $\delta x_0$ , is finite. The deviation vector,  $\delta x_0^*$ , is a Karush-Kuhn-Tucker point of the Lagrangian, which maximizes or minimizes the Lagrangian

$$\nabla L_k(\delta x_0^*) = \mathbf{0} \quad (5)$$

Approved for public release; distribution is unlimited. Public Affairs release approval #AFRL-2022-4065. The views expressed are those of the authors and do not reflect the official guidance or position of the United States Government, the Department of Defense or of the United States Air Force.

$$L_k = \frac{\tilde{\Phi}^{(k)} \delta x_0^k}{\tilde{\Phi}^{(2)} \delta x_0^2} - \sigma \left( \tilde{\Phi}^{(2)} \delta x_0^2 - \beta \right). \quad (6)$$

The value of the  $\beta$  constraint does not need specification as it is placed without loss of generality.

The constraint is posed so that the following substitution is made to optimize for  $z$  instead of  $\delta x_0$  as

$$\delta x_0 = \left( \Phi^{(2)} \right)^{-1} z. \quad (7)$$

The substitution can also be taken as performing a linear transformation that allows for numerical stability and facilitates computation without affecting the nonlinearity of the model as described in [3].

$$L_k = \frac{\tilde{\Phi}^{(k)} \left( \left( \Phi^{(2)} \right)^{-1} z \right)^k}{z^T z} - \sigma \left( z^T z - \beta \right) \quad (8)$$

$$L_k = \frac{\check{\Phi}^{(k)} z^k}{z^T z} - \sigma \left( z^T z - \beta \right) \quad (9)$$

The numerator of the first term of Eq.(8) is provided by  $\check{\Phi}^{(k)} z^k$ . The procedure continues by replacing  $\check{\Phi}^{(k)} z^k$  with a supersymmetric tensor  $\check{\mathcal{S}}^{(k)}$  to simplify computations. Furthermore,  $\|z\|$  and  $\hat{z}$  are separated and  $L_k$  is multiplied by  $\hat{z}^T \hat{z}$ , where the gradient of  $L_k$  with respect to  $\hat{z}$  is set to zero,

$$\nabla_{\hat{z}} L_k = k \check{\mathcal{S}}^{(k)} \hat{z}^{k-1} \|z\|^{k-2} - 2\sigma \|z\|^2 \hat{z} = 0. \quad (10)$$

To simplify Eq.(10),  $\lambda$  is introduced, and  $(\lambda, \hat{z})$  forms the Z-eigenpair of  $\check{\mathcal{S}}^{(k)}$ . Each eigenvector produces a stationary point of the Lagrangian. Moreover, the eigenpair that maximizes the Lagrangian corresponds to the eigenvalue with the largest magnitude  $(\lambda_k^*, \hat{z}_k^*)$ ,

$$L_k^* = \check{\mathcal{S}}^{(k)} z_k^* \|z_k^*\|^{k-2} \quad (11)$$

$$= \lambda_k^* \|z_k^*\|^{k-2}. \quad (12)$$

The eigen vector  $z_k^*$  describes the direction of strong nonlinearity from the parameter  $z$ . From the original substitution relationship in Eq.(7), this result can be written in original parameters as shown in Eq.(13). Note that  $\alpha$  is the magnitude of  $\delta x$ , which can be scaled independently.

$$\delta \hat{x}_k^* = \frac{\left( \Phi^{(2)} \right)^{-1} \hat{z}_k^*}{\left\| \left( \Phi^{(2)} \right)^{-1} \hat{z}_k^* \right\|} \quad (13)$$

$$\|z_k^*\| = \left\| \Phi^{(2)} \delta \hat{x}_k^* \right\| \alpha \quad (14)$$

From the results formulated above, the TEMoN is then computed from tensor eigenpairs. The  $k$ th-order model nonlinearity is maximized by vector  $\delta \hat{x}_k^*$ ,

$$\tau_k = \left| \lambda_k^* \right| \left\| \Phi^{(2)} \delta \hat{x}_k^* \right\|^{k-2} \alpha^{k-2} \quad (15)$$

$$\text{TEMoN}_{\Phi, m} = \sum_{k=3}^m \tau_k. \quad (16)$$

Approved for public release; distribution is unlimited. Public Affairs release approval #AFRL-2022-4065. The views expressed are those of the authors and do not reflect the official guidance or position of the United States Government, the Department of Defense or of the United States Air Force.

The scalar  $\lambda_k^*$  is the largest-magnitude Z-eigenvalue of supersymmetric tensor  $\check{S}^{(k)}$ , given  $k$  is the tensor order. The vector  $\delta\hat{x}_k^*$  is computed from the eigenvector  $z_k^*$ . An important feature in Eq.(15) shows that the magnitude of  $\delta\hat{x}_k^*$  for  $k \geq 3$  has the same value as  $\alpha$ , which is independent of the eigenpair computation. This allows one to set a deviation magnitude,  $\sqrt{Tr(\mathbf{P})}$ , that is related to the initial covariance. The origin of the system is defined at its barycenter, such that the largest body with mass  $m_1$  and second largest body with mass  $m_2$  are always on the x-axis. The positive x-direction is from the origin to the second body, and the y-axis is aligned with the velocity vector of the second body. The three-body gravitational parameter  $\mu$  shown by

## 2.2 Propagation and CRTBP

The Circular Restricted Three-Body Problem is a simplified multi-body dynamics model that applies two constraints to the generalized Three-Body Problem. The first is that the motion of the two primary bodies about their common barycenter is constrained to a circular orbit, and the second is that the mass of the third object (i.e. a spacecraft) is negligible compared to the masses of the primaries. It is useful to analyze and visualize this system with respect to the rotating synodic frame, with the origin at the system barycenter, the x-axis directed from the barycenter towards the smaller mass ( $m_2$ ) and y-axis directed along the velocity vector of  $m_2$ . The three-body gravitational parameter  $\mu$  shown by

$$\mu = \frac{m_2}{m_1 + m_2}. \quad (17)$$

The non-dimensional mass of second-largest body is then equal to  $\mu$  and the mass of the largest body is  $1 - \mu$ . One nondimensional length unit (LU) is equal to the distance between the two primaries. Therefore, the distance from the origin to  $m_1$  is  $-\mu$  LU and the distance from origin to  $m_2$  is  $(1 - \mu)$  LU. The time unit (TU) is set so that the periods of the orbits of the primary bodies is  $2\pi$  TU. The equations of motion for the CRTBP from [15] are

$$\ddot{x} - 2\dot{y} = x - (1 - \mu)\frac{x + \mu}{r_1^3} - \mu\frac{x + \mu - 1}{r_2^3} \quad (18)$$

$$\ddot{y} + 2\dot{x} = \left(1 - \frac{1 - \mu}{r_1^3} - \frac{\mu}{r_2^3}\right)y \quad (19)$$

$$\ddot{z} = \left(\frac{\mu - 1}{r_1^3} - \frac{\mu}{r_2^3}\right)z \quad (20)$$

$$\text{where } r_1 = \sqrt{(x + \mu)^2 + y^2 + z^2} \quad \text{and} \quad r_2 = \sqrt{(x + \mu - 1)^2 + y^2 + z^2} \quad (21)$$

The position and velocity of the third body in the CRTBP are represented with the state vector  $\mathbf{x}(t)$  and its time derivative is  $\mathbf{f}(\mathbf{x}(t), t)$

$$\mathbf{x}(t) = [x \quad y \quad z \quad \dot{x} \quad \dot{y} \quad \dot{z}]^T \quad \mathbf{f}(\mathbf{x}(t), t) = [\dot{x} \quad \dot{y} \quad \dot{z} \quad \ddot{x} \quad \ddot{y} \quad \ddot{z}]^T \quad (22)$$

## 3. GAUSSIAN DISTRIBUTION MEASURES

### 3.1 Uncertainty Propagation

A multivariate Gaussian Probability Density Function (PDF) at initial time  $t_{k=0}$  is represented using the first and second moment of a random variable  $\mathbf{x}$  and denoted by

$$p(\mathbf{x}; \mathbf{m}, \mathbf{P}) = \frac{1}{|2\pi\mathbf{P}|^{1/2}} \exp\left\{-\frac{1}{2}(\mathbf{x} - \mathbf{m})^T \mathbf{P}^{-1}(\mathbf{x} - \mathbf{m})\right\}. \quad (23)$$

The first moment or mean is denoted by  $\mathbf{m}$  and second moment or covariance is  $\mathbf{P}$ . The mean,  $\mathbf{m} \in \mathbb{R}^n$ , contains  $n$  parameters including at least six for position and velocity, and the covariance must be symmetric and positive definite.

From the work presented in [19], the sigma-point filter relies on the weighted statistical linear regression from [12]. It utilizes the construction of sigma-points and respective weights from the Gaussian first and second moment. Each

Approved for public release; distribution is unlimited. Public Affairs release approval #AFRL-2022-4065. The views expressed are those of the authors and do not reflect the official guidance or position of the United States Government, the Department of Defense or of the United States Air Force.

sigma-point is then propagated through a nonlinear function, which in this case consists of the nonlinear dynamics of the Circular-Restricted-Three-Body Problem (CRTBP). Then an approximate Gaussian representation is formed from the sigma-points. This is utilized to observe the motion of the sigma-points relative to its Gaussian representation and to propagate the uncertainty.

The symmetric and unscaled sigma-point implementation has proven successful in processing real space object data shown in [18]. Moreover, the unscaled version reduces the number of parameters to tune, while achieving robustness and improved results for the Unscented Kalman Filter (UKF). The set of sigma-points,  $\mathcal{X}_j$ , is formulated as

$$\mathcal{X}_0 = \mathbf{m}_0 \quad (24)$$

$$\mathcal{X}^{(i)} = \mathbf{m}_0 + \sqrt{n} \left[ \sqrt{\mathbf{P}_0} \right]_i \quad (25)$$

$$\mathcal{X}^{(i+n)} = \mathbf{m}_0 - \sqrt{n} \left[ \sqrt{\mathbf{P}_0} \right]_i. \quad (26)$$

The scale factor is  $\sqrt{n}$ , where  $n$  is the number of parameters in the state. The term  $\left[ \sqrt{\mathbf{P}_0} \right]_i$  represents the  $i$ th column of the Cholesky decomposition from initial covariance  $\mathbf{P}_0$ . The weights for the sigma-points are defined by  $w_j = \frac{1}{2n}$  for all sigma-points  $j = 1 \dots 2n + 1$ . The sigma-points are propagated from time-step  $k - 1$  to  $k$  using the nonlinear differential equations of the CRTBP:

$$\dot{\mathcal{X}}_j(t) = \mathbf{f}(\mathcal{X}_j(t), t), \quad \mathcal{X}_j(t_{k-1}) = \mathcal{X}_{j,k-1}. \quad (27)$$

At each time step  $t_k$ , the mean,  $\mathbf{m}_k$ , and covariance,  $\mathbf{P}_k$ , are approximated from the sigma-points using part of the Unscented Transform process

$$\mathbf{m}_k = \sum_{j=0}^{2n} w_j \mathcal{X}_{j,k} \quad (28)$$

$$\mathbf{P}_k = \left\{ \sum_{j=0}^{2n} w_j (\mathcal{X}_{j,k} - \mathbf{m}) (\mathcal{X}_{j,k} - \mathbf{m})^T \right\} + \mathbf{Q}_k, \quad (29)$$

where the process noise matrix  $\mathbf{Q}_k$  is defined by

$$\mathbf{Q}_k = \begin{bmatrix} \frac{\Delta t^4}{4} \sigma_f^2 & 0 & 0 & \frac{\Delta t^3}{2} \sigma_f^2 & 0 & 0 \\ 0 & \frac{\Delta t^4}{4} \sigma_f^2 & 0 & 0 & \frac{\Delta t^3}{2} \sigma_f^2 & 0 \\ 0 & 0 & \frac{\Delta t^4}{4} \sigma_f^2 & 0 & 0 & \frac{\Delta t^3}{2} \sigma_f^2 \\ \frac{\Delta t^3}{2} \sigma_f^2 & 0 & 0 & \Delta t^2 \sigma_f^2 & 0 & 0 \\ 0 & \frac{\Delta t^3}{2} \sigma_f^2 & 0 & 0 & \Delta t^2 \sigma_f^2 & 0 \\ 0 & 0 & \frac{\Delta t^3}{2} \sigma_f^2 & 0 & 0 & \Delta t^2 \sigma_f^2 \end{bmatrix}, \quad (30)$$

with  $\Delta t$  describing the difference between time  $t_k$  and  $t_0$  and  $\sigma_f^2$  is the variance associated with the acceleration term. In a simulation, the value  $\sigma_f$  can be tuned to provide a realistic covariance matrix and low state errors.

### 3.2 Differential Entropy and Evolutionary Deviation of the Mahalanobis Distance

In addition to the TEMoN, which describes the dynamics of the cislunar regime, an additional set of measures which characterize the Gaussian distribution may provide insight into changes in the uncertainty due to both dynamic effects and the cumulative effect of time. The idea of identifying non-Gaussian behavior stems from [6], [7] and [8], where an information metric such as differential entropy or Shannon entropy is utilized to compare its linearized prediction and the nonlinear result. A deviation large enough, as indicated by a threshold, signifies strong nonlinear effects. This can be used to provide an update to the Gaussian distribution representation through the addition of Gaussian Mixture Model components. In this study, we seek to find a range of thresholds to predict the transition from Gaussian to non-Gaussian

behavior. We utilize two major metrics for this section, the differential entropy and Evolutionary Deviation of the Mahalanobis distance (EDM).

The differential entropy is defined by [17] and shown as

$$H(\mathbf{x}) = \int_{\mathcal{P}} p(\mathbf{x}) \log(p(\mathbf{x})) dx = E\{-\log p(\mathbf{x})\}, \quad (31)$$

where  $\mathbf{x} \in \mathbb{R}^n$  is the state of the system defined by position and velocity ( $n = 6$ ) and  $p(\mathbf{x})$  is the PDF. From the superset of  $p(\mathbf{x})$ , the differential entropy gives the average amount of information content on the given random variable as explained by [6] and [17]. The application of Eq.(31) to a Gaussian PDF results in

$$H(\mathbf{x}) = \frac{1}{2} \log |2\pi e \mathbf{P}|, \quad (32)$$

where it simply relates the covariance to entropy with the logarithm of base ( $e$ ). Therefore, the differential entropy at each time-step, given covariance propagated with sigma-points,  $\mathbf{P}_k$ , is

$$H_k = \frac{1}{2} \log |2\pi e \mathbf{P}_k|. \quad (33)$$

The metric based on differential entropy is computed using the change in differential entropy from time  $t_0$  to  $t_k$ , divided by the value at  $t_0$ , which is represented by  $\Delta H/H_0$ .

The EDM metric depends on the evolution of the maximum sigma-point Mahalanobis distance. The sigma-points are not re-sampled but rather continuously propagated throughout the various trajectories. The behavior of the sigma-points is observed by obtaining  $\mathcal{M}_{j,k}$ , the Mahalanobis distance (MD) of sigma-point  $j$  to the respective mean  $\mathbf{m}_k$  from Eq.(28) at time  $t_k$ .

$$\mathcal{M}_{j,k} = \kappa_{j,k}^2 = [\mathcal{X}_{j,k} - \mathbf{m}_k]^T \mathbf{P}_k^{-1} [\mathcal{X}_{j,k} - \mathbf{m}_k] \quad (34)$$

At time  $t_0$ , the initial MD for all points,  $\mathcal{M}_{j,k=0}$ , should be equal to state size  $n$  when using the unscaled sigma-points. That is because all of the sigma-points lie on the surface of the same probability ellipsoid. At any other time, the MD values will start to vary from the initial MD as the sigma points begin to deviate slightly and no longer lie on the same Gaussian probability ellipsoid. The value,  $MD_k^*$ , is computed using the maximum absolute value of the change in MD.

$$MD_k^* = \max \frac{|\mathcal{M}_{\forall j} - \mathcal{M}_{\forall j,k=0}|}{\mathcal{M}_{\forall j,k=0}} \quad (35)$$

Thus, for each timestep  $k$  for which a sigma-point is propagated, the MD is computed in relation to the propagated  $\mathbf{m}$  and  $\mathbf{P}$ .

### 3.3 Monte Carlo Based Methods

The Cramér-von Mises (CVM) metric was suggested in [10] and also applied by in [1]. This metric is used to determine when the uncertainty becomes non-Gaussian. When the uncertainty is represented by a PDF, the CVM,  $\omega^2$ , has an analytic representation

$$\omega^2 = \int_0^{\kappa^m} [F_n(\kappa^2) - F^*(\kappa^2)]^2 dF^*. \quad (36)$$

where  $F^*(\kappa)$  is the ideal cumulative distribution function (CDF) of the MD and  $F_n(\kappa^2)$  is the approximate CDF of the MD, for  $n$  degrees of freedom. For Monte Carlo results, the individual sample  $i$  for  $m$  samples are processed with

$$\omega^2 = \frac{1}{12m} + \sum_{i=1}^m \left[ \frac{2i-1}{2m} - F(\kappa_i^2) \right]^2 \quad (37)$$

where

Approved for public release; distribution is unlimited. Public Affairs release approval #AFRL-2022-4065. The views expressed are those of the authors and do not reflect the official guidance or position of the United States Government, the Department of Defense or of the United States Air Force.

$$\kappa_i^2 = [x_i - \mathbf{m}_k]^T \mathbf{P}_k^{-1} [x_i - \mathbf{m}_k] \quad (38)$$

The value  $F(\kappa_i^2)$  is the CDF of the MD for the given Monte Carlo sample  $x_i$  obtained using Eq.(38). Note that the values of  $\kappa_i^2$  are sorted in increasing order and the CDF is computed for a chi-squared distribution  $\chi^2(n)$ . Table 1 shows the range of the CVM as a function of the confidence factor  $(1 - \alpha)$  [1][10]. For example, to achieve a 99.9% probability that the uncertainty is Gaussian, the threshold required is  $\omega^2 < 1.16204$ .

Sample Size	1- $\alpha$			
$\infty$	90%	95%	99%	99.9%
	[0,0.34730]	[0,0.46136]	[0, 0.74346]	[0, 1.16204]

Table 1: CVM Metric Range as a function of the Confidence Level from [1].

Another metric, called percent-within (PW), uses a probability ellipsoid computed from the covariance and counts how many Monte Carlo sample points are within that ellipsoid. To compute PW, the MD value from each Monte Carlo sample point is computed and counted with the following formulation

$$c_i = \begin{cases} 1, & \text{if } \kappa^2(x_i) \leq \gamma_{(1-\alpha),n} \\ 0, & \text{otherwise} \end{cases}, \quad (39)$$

if  $\kappa_i^2 < \gamma_{(1-\alpha),n}$ , then the sample is counted with  $c_i = 1$ . The value  $\gamma_{(1-\alpha),n}$  is computed for a chi-squared distribution given the desired confidence factor  $(1 - \alpha)$  of the probability ellipsoid and the number of degrees of freedom. This counting process for each sample point is represented by  $c_i$ . The non-zero  $c_i$  are summed and normalized with the total number of samples available and presented as a percentage,

$$PW = \frac{\sum_{i=1}^m c_i}{m} 100\%. \quad (40)$$

This metric provides quantification of the sample points within the confidence factor criteria, monitoring the transition of the sample points relative to boundary  $\gamma_{(1-\alpha),n}$ .

### 3.4 Multivariate Gaussian Particle Cloud

The Monte Carlo methods rely on a large number of samples because of the dimension of the state,  $n \geq 6$ , but the computation required for each sample can prove expensive. To reduce the number of samples needed in a particle cloud, but still accurately represent the PDF, the sample states are optimized using a set of requirements. The CVM for each individual component,  $\omega_i^2$ , of the state is minimized as well as the CVM for the full-state Mahalanobis distance,  $\omega^2$ . The skewness,  $b_{1,p}$ , is also minimized. Each value in the covariance computed from the Monte Carlo points,  $\hat{\mathbf{P}}$ , is optimized to match the corresponding values in the desired covariance,  $\mathbf{P}$ .

To generate a population of  $m$  points to represent a covariance of dimension  $n$ , the first step is to create an initial distribution of points to be optimized. To do so, an initial Gaussian with no correlations and all unit variances are used. (i.e. the covariance matrix is equal to the identity matrix). Generating these initial points using normally distributed random numbers was found to result in too uneven of a distribution with gaps and clumps. To ensure an even distribution, it is divided into a grid over only positive values with an interval,  $\Delta x$ , of 1. The maximum size for each dimension of the grid is set using the radius of a sphere with a probability of  $1 - \frac{1}{m}$  as computed from a  $\chi^2(n)$  distribution. The resulting density for a given grid interval would be

$$\rho = \frac{1}{\Delta x^n}. \quad (41)$$

For a three-dimensional case, point  $j$  in the grid is called  $\mathbf{X}_j$  and is

$$\mathbf{X}_j = [x_j, y_j, z_j]^T = [X_{j,0}, X_{j,1}, X_{j,2}]^T. \quad (42)$$

For the points in the grid where each component is less than or equal to the succeeding component, the desired density is computed using the PDF from Eq.(23), multiplied by  $m$ . The PDF is computed using the identity covariance matrix

and assuming the mean is zero. If placed by

$$\frac{1}{\Delta x^n} > m \cdot p(\mathbf{X}_j) \quad (43)$$

then a sample point is placed at that grid location  $\mathbf{X}_j$ . Also, points are placed at all the possible reflections of the permutations of that state. For example, if  $n = 3$  and  $\mathbf{X}_j = [0, 1, 1]$ , then all the permutations of that state would be

$$[0, 1, 1] \quad [1, 1, 0] \quad [1, 0, 1].$$

All the reflections of those states would be

$$\begin{array}{ccc} [0, 1, 1] & [1, 1, 0] & [1, 0, 1] \\ [0, -1, 1] & [-1, 1, 0] & [-1, 0, 1] \\ [0, 1, -1] & [1, -1, 0] & [1, 0, -1] \\ [0, -1, -1] & [-1, -1, 0] & [-1, 0, -1] \end{array}$$

After all grid points have been checked in this way, the grid interval  $\Delta x$  is reduced by half, which increases  $\rho$ . Then the process is repeated, except that any grid points which have already been checked previously are skipped. The process continues until  $n$  points have been generated. The realized sample covariance,  $\hat{\mathbf{P}}$  shown below

$$\hat{\mathbf{P}} = \frac{1}{n} \sum_{j=0}^{n-1} \mathbf{X}_j \mathbf{X}_j^T, \quad (44)$$

should be optimized to match the desired covariance,  $\mathbf{P}$ . For each component of the state, the Cramér-von Mises statistic is computed after sorting all the values of that component and then processing them in ascending order:

$$\omega_i^2 = \frac{1}{12m} + \sum_{j=0}^{n-1} \left[ F(X_{j,i}) - \frac{2j+1}{2m} \right]^2. \quad (45)$$

CDF or  $F(X_{j,i})$  is the cumulative distribution function for value  $X_{j,i}$  for a zero mean, one-dimensional Gaussian distribution with a standard deviation of one. Note that the counting process is from 0 to  $n - 1$  instead of 1 to  $n$ , so the equation is slightly different than in [10]. Also, the fixed term  $\frac{1}{12m}$  is dropped since it cannot be minimized.

For example, the Cramér-von Mises statistic for the  $x$ -component,  $\omega_0^2$ , is computed by taking the  $x$  components for all  $m$  points and sorting them in ascending order before computing the statistic. For  $\omega^2$ , the full-state Cramér-von Mises statistic, the Mahalanobis distance,  $\kappa_j^2$ , is computed for each point  $j$ . Since the covariance is the identity matrix,

$$\kappa_j^2 = \sum_{i=0}^{m-1} X_{j,i}^2 \quad (46)$$

$\omega^2$  is computed after sorting all the  $\kappa_j^2$  values and then processing them in ascending order from Eq.(45). Where in this case, the CDF  $F(\kappa_j^2)$  is the cumulative distribution function of an  $n$ -dimensional  $\chi^2$  distribution. Once again, the  $\frac{1}{12m}$  term is dropped. The skewness,  $b_{1,p}$ , is computed using the equation as shown in [4], simplified for zero mean state  $\bar{\mathbf{X}}$ , and identity covariance  $P$  matrix:

$$b_{1,p} = \frac{1}{m^2} \sum_{j=0}^{m-1} \sum_{k=0}^{m-1} [\mathbf{X}_j^T \mathbf{X}_k]^3. \quad (47)$$

To optimize the particle cloud, a differential correction process is applied to the sample points so that the realized vector of statistics  $\hat{\mathbf{Y}}$  matches desired statistics. The vector of statistics  $\hat{\mathbf{Y}}$  is composed of the covariance components, the CVM for each component  $\omega_i^2$ , the CVM for full-state  $\omega^2$ , and the skewness  $b_{1,p}$ . The desired  $\mathbf{Y}$  should be composed of ones for diagonal components of the covariance matrix and zeros for the rest. Thus, the residual vector  $\mathbf{y}$  is

$$\mathbf{y} = \mathbf{Y} - \hat{\mathbf{Y}} \quad (48)$$

Approved for public release; distribution is unlimited. Public Affairs release approval #AFRL-2022-4065. The views expressed are those of the authors and do not reflect the official guidance or position of the United States Government, the Department of Defense or of the United States Air Force.

To minimize the squares of the residuals, the points are differentially corrected using a partials matrix  $H$  which is  $\partial\hat{\mathbf{Y}}/\partial\mathbf{X}$ . The partials for point  $j$ , component  $i$  are

$$\frac{\partial\hat{P}_{i,i}}{\partial X_{j,i}} = \frac{2X_{j,i}}{m}, \quad \frac{\partial\hat{P}_{k,i}}{\partial X_{j,i}} = \frac{X_{j,k}}{m}, k \neq i \quad (49)$$

$$\frac{\partial\hat{P}_{k,k}}{\partial X_{j,i}} = 0, k \neq i, \quad \frac{\partial\hat{P}_{k,\ell}}{\partial X_{j,i}} = 0, k \neq i, \ell \neq i \quad (50)$$

$$\frac{\partial\omega_i^2}{\partial X_{j,i}} = 2 \left[ F(X_{j,i}) - \frac{2j+1}{2m} \right] p(X_{j,i}), \quad \frac{\partial\omega_k^2}{\partial X_{j,i}} = 0, k \neq i \quad (51)$$

$$\frac{\partial\omega^2}{\partial X_{j,i}} = 4X_{j,i} \left[ F(\kappa_j^2) - \frac{2j+1}{2m} \right] p(\kappa_j^2), \quad \frac{\partial b_{1,p}}{\partial X_{j,i}} = \frac{3}{m^2} \sum_{k=0}^{m-1} X_{k,i} [\mathbf{X}_j^T \mathbf{X}_k]^2 \quad (52)$$

Note that the derivative of the CDF is the PDF and

$$\frac{\partial\omega^2}{\partial X_{j,i}} = \frac{\partial\omega^2}{\partial\kappa_j^2} \cdot \frac{\partial\kappa_j^2}{\partial X_{j,i}} \quad (53)$$

$$\frac{\partial\omega^2}{\partial\kappa_j^2} = 2 \left[ F(\kappa_j^2) - \frac{2j+1}{2m} \right] p(\kappa_j^2). \quad (54)$$

When the covariance is an identity matrix then

$$\frac{\partial\kappa_j^2}{\partial X_{j,i}} = 2X_{j,i}. \quad (55)$$

Next, a correction to solve for  $\mathbf{X}$  denoted by  $\hat{\mathbf{x}}$ . The correction vector  $\hat{\mathbf{x}}$  must be found using the minimum norm solution since there are more estimated parameters than equations to be solved:

$$\hat{\mathbf{x}} = H^T [H \cdot H^T]^{-1} \mathbf{y}. \quad (56)$$

The correction  $\hat{\mathbf{x}}$  is added to the estimated state vector  $\mathbf{X}$  and the process is repeated. The final step is to scale and rotate the points using the desired covariance matrix, which can be decomposed into

$$\mathbf{P} = \mathbf{V} \mathbf{D} \mathbf{V}^T, \quad (57)$$

where  $\mathbf{V}$  is a matrix with the eigenvectors in the columns.  $\mathbf{D}$  is a diagonal matrix with the eigenvalues along the diagonal,  $\sigma_{p,i}^2$ , which are the variances in the principal axis frame.

$$\mathbf{D} = \begin{bmatrix} \sigma_{p,0}^2 & & \\ & \ddots & \\ & & \sigma_{p,n-1}^2 \end{bmatrix} \quad (58)$$

In this case, the matrix  $\mathbf{V}$  is a rotation from the principal axis frame to the frame used by  $\mathbf{P}$ . Each point  $\mathbf{X}_j$  is scaled and rotated to have the proper variances and covariances and becomes  $\mathbf{X}_j^*$  by the following:

$$\mathbf{X}_j^* = \mathbf{V} \begin{bmatrix} \sigma_{p,0} X_{j,0} \\ \vdots \\ \sigma_{p,n-1} X_{j,n-1} \end{bmatrix}. \quad (59)$$

The complete set of estimated parameters cannot be simultaneously satisfied with a finite number of points, so a second step can be performed to optimize just the parameters which are most important. The only exception is that the covariance and skewness can both be satisfied at the same time. If the single-component Cramér-von Mises statistics,  $\omega_i^2$ , are the only parameters which are prioritized, the point components are set to the values which match the ideal CDF directly. If  $\omega^2$ , the full-state Cramér-von Mises statistic, is the only parameter to be prioritized, the points are iteratively corrected one at a time until the  $\kappa_j^2$  value matches the ideal value from the  $\chi^2$  CDF.

## 4. ORBIT ANALYSIS AND RESULTS

### 4.1 Orbit Families

A few families of periodic orbits for the CRTBP were selected to apply the TEMoN and Gaussian distribution measures. Each orbit family in Table 2 is subdivided into orbits, each with an index between 1 and 512, where each corresponds to a different orbit period.

Designation	Definition
$L_i$	Libration Point ( $i = 1, \dots, 5$ )
$L_i$	The planar Lyapunov family from $L_i$ ( $i = 1, 2, 3$ )
$L_i$	The Long-Period planar family from $L_i$ ( $i = 4, 5$ )
$H_i$	Halo family from $L_i$ at $L_i$ ( $i = 1, 2, 3$ )
DRO	Distant Retrograde Orbits

Table 2: Subset of elemental orbit families from [9] with DRO family from [20].

A few examples of these orbit indices are shown in Fig. 1, where the visualization for  $H1$  and  $H2$  are split into northern and southern subsets. The color on each orbit of each plot provides context for the orbit period captured in days and where it resides in the cislunar space. The libration points  $L_1$  and  $L_2$  are shown in plots for  $H1$  and  $H2$ . For the plots  $L1$ ,  $L2$  and DRO the points  $L_1$  to  $L_5$  are displayed except for  $L_3$ . The plots  $L4$  and  $L5$  show all libration points.

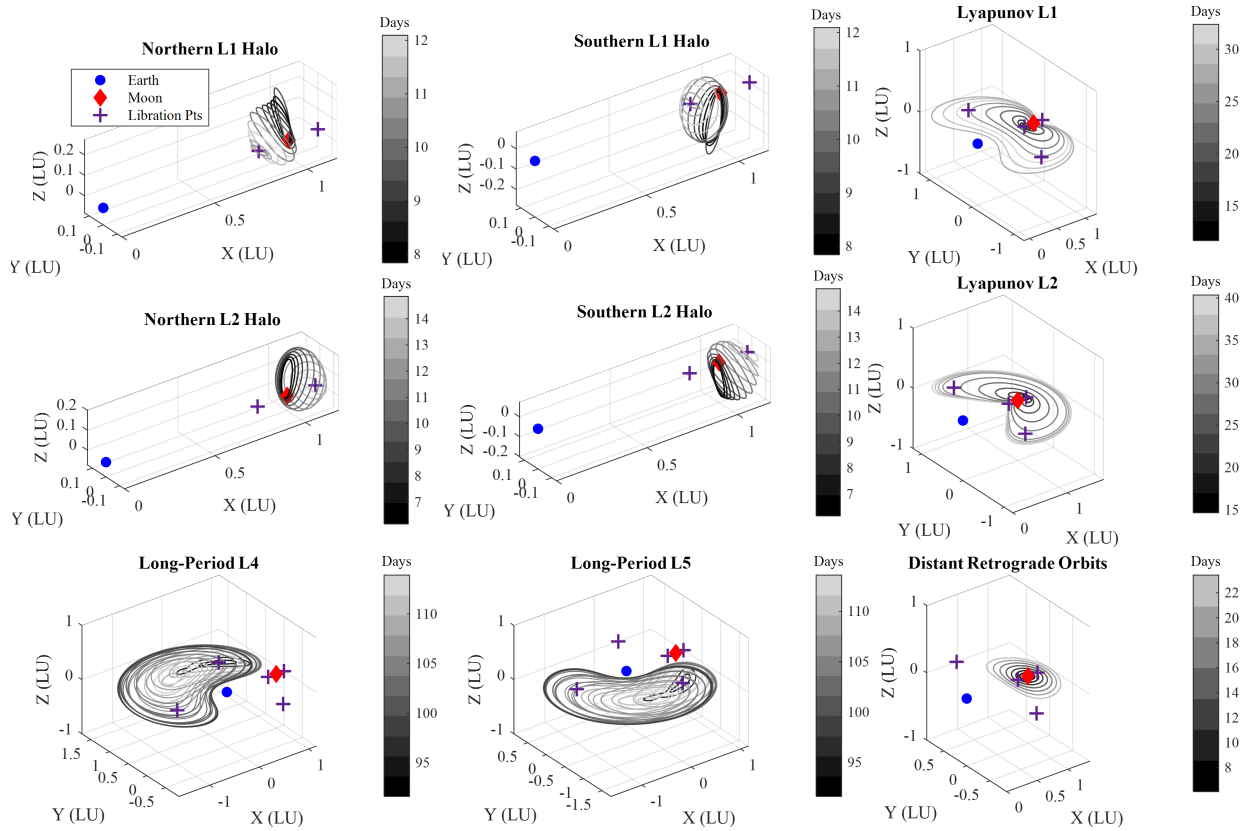


Fig. 1: Illustration of the subset of elemental orbit families from Table 1 from [9] and DRO family from [20] in the synodic frame. (upper left to lower right)  $H1$  (North/South),  $L1$ ,  $H2$  (North/South),  $L2$ ,  $L4$ ,  $L5$  and DRO.

Approved for public release; distribution is unlimited. Public Affairs release approval #AFRL-2022-4065. The views expressed are those of the authors and do not reflect the official guidance or position of the United States Government, the Department of Defense or of the United States Air Force.

## 4.2 Application and Methods

To determine a link between non-linearity quantified by TEMoN and evolution into non-Gaussian uncertainty, metrics such as the CVM and PW described in Section 3.3 are employed. They allow one to quantify how Gaussian a distribution is in reference to a non-linear measure. Then a selection process for a TEMoN threshold can be performed, which in turn predicts when the trajectory is likely to become non-Gaussian. In addition, the Gaussian distribution measures from Section 3.2 can be used to predict the transition of the uncertainty from Gaussian to non-Gaussian. Those measures have a lower computational cost, and their reliability will be compared with that of TEMoN.

It is recommended that  $10^n$  Monte Carlo samples should be used to represent an  $n$ -dimensional system, but in this case that would lead to excessive computation time. This analysis uses 10,000 samples obtained using the optimized particle cloud presented in Section 3.4. Compared to the same number of randomly drawn samples, the optimized particle cloud samples show a less clumpy distribution throughout the region of interest with better coverage of the edges. The set of sigma-points described in Eq.(24-26) are generated from the same initial  $\mathbf{m}_0$  and  $\mathbf{P}_0$ . In regards to the TEMoN metric presented in section 2.1, the analysis utilizes a 4<sup>th</sup>-order STT. The deviation is related to the square root of the trace of the initial covariance  $|\delta x_0| = \sqrt{\text{Tr}(\mathbf{P}_0)}$ . For this study the position standard deviation and velocity are  $\sigma_r = 10$  km and  $\sigma_v = 1 \cdot 10^{-4}$  km/s.

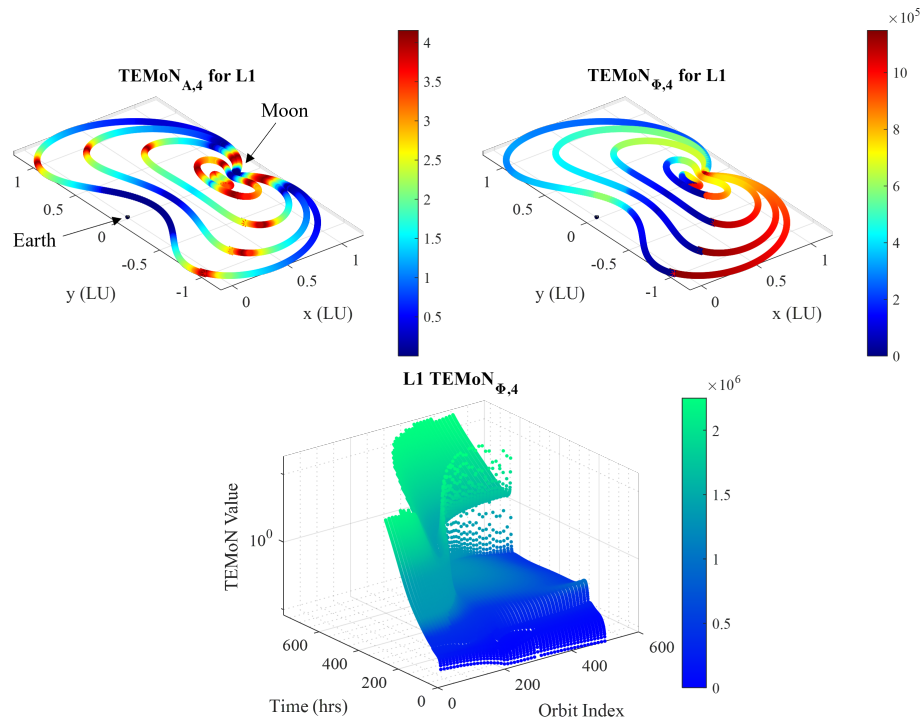


Fig. 2: (left) LDT TEMoN<sub>A</sub> for sparse sets of orbits within the L1 family. (right) STT TEMoN<sub>Φ</sub> for the same sparse set of orbits, comparing differences in LDT and STT TEMoN. (bottom) TEMoN<sub>Φ,4</sub> over the orbit indices from 10 to 500 in increments of 10. TEMoN order parameter  $m = 4$  and deviation magnitude  $|\delta x_0| = 1.752 \cdot 10^{-3}$ .

For each orbit within a family, the 10,000 Monte Carlo samples and set of sigma-points are propagated for one period. For each time-step, the mean  $\mathbf{m}_k$  and covariance  $\mathbf{P}_k$  are approximated by Eq.(28-29) from the sigma-points, which allows one to compute the  $MD_k^*$  and  $H_k$ . The CVM,  $\omega_k^2$ , and PW metrics,  $PW_k$ , are also obtained. To compute the TEMoN<sub>Φ</sub>, the generation of supersymmetric tensors and the tensor eigenpair computation are done with the help of the Tensor toolbox [2] as seen in [11]. To determine peaks of non-linearity based on the current state dynamics in cislunar space (as opposed to the solution flow over time), the TEMoN for the Local Dynamic Tensors, TEMoN<sub>A</sub>, is also computed for a sparse set of orbits within each family. An example of the TEMoN values for both STT and LDT methods are shown in Fig. 2.

The right and bottom plots of Fig. 2 show that TEMoN<sub>Φ</sub> values can span across several orders of magnitude for the L1

family. The bottom plot of Fig. 2 shows a surface of TEMoN values according to propagation time and orbit index. As the orbit index increases in the L1 family, the orbit period increases along with the proximity to the Moon and Earth as seen in Fig. 2, causing development of sharp peaks. Due to intricate structure on the surface, the selection of a threshold for TEMoN may prove difficult. Thus, consistency in finding the limit of Gaussian behavior using PW is particularly important. The contrast between  $TEMoN_{\Phi}$  and  $TEMoN_A$  is also interesting. The LDT is affected by the magnitude of the deviation  $|\delta x_0|$ , and peaks represent highly nonlinear dynamics and arise in certain regions of the trajectories. In those same regions, STT also increases rapidly. However, since STT is cumulative, it is also dependent on time of propagation.

The  $PW_k$  metric is computed at each time step  $t_k$  using a confidence interval corresponding to a 99.9% probability. If the PW reaches below this threshold,  $PW_k < 99.9\%$ , the  $TEMoN_{\Phi,4}$  is captured for that time. For the CVM approach, the threshold for 99.9% is provided in Table 1 from [1], such that when the computed CVM breaches the threshold  $\omega_k^2 < 1.16204$ , then  $TEMoN_{\Phi}$  is captured. This comparison is shown in Fig. 3 depicting the threshold values for each individual orbit in the family in each curve. The TEMoN values obtained using the PW threshold provide a more consistent range across orbit families. The PW also allows control of the resolution for a given number of Monte Carlo particles. If the number of particles decreases or increases, the threshold in PW can be adjusted to capture greater precision or sensitivity. In addition, to counter the noise produced by the motion of individual sample points near the 99.9% boundary, a backward-biased smoothing technique is applied to properly capture sudden changes in PW. Each point in the TEMoN curves represents the non-linearity measure at the time along the propagated trajectory when the uncertainty distribution is no longer Gaussian. In a similar way, the EDM metric  $MD^*$  and differential entropy  $H$  are captured at the same time the TEMoN threshold was captured.

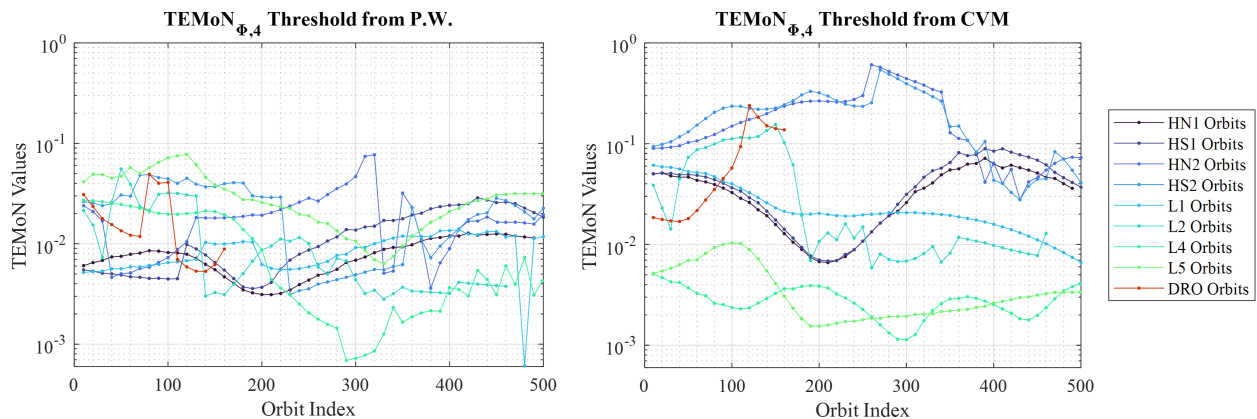


Fig. 3: The plot on the left represents the TEMoN threshold values based on the PW metric. The plot on the right provides the TEMoN threshold values based on the CVM metric.

For the L1 family, the right and bottom plots of Fig. 2 show that  $TEMoN_{\Phi}$  values can span several orders of magnitude. This varies for the different orbit families and propagation times described in Section 4.3. In bottom plot of Fig. 2, a surface shows TEMoN values for each orbit in the family for various propagation times. As the orbit index increases in the L1 family, the orbit period increases and the distances to the Moon and Earth decrease during close approaches. Those close approaches often lead to sharp peaks or increases in nonlinearity as measured by TEMoN. The steep slopes and sharp peaks on the surface show that the selection of a TEMoN threshold may prove difficult. Thus, consistency in selection of  $TEMoN_{\Phi}$  values when triggered by the PW metric is particularly important. The top two plots show the difference between  $TEMoN_{\Phi}$  and  $TEMoN_A$ . The LDT peaks ( $TEMoN_A$ ) arise in certain regions of the trajectories with highly nonlinear dynamics and can be affected by the initial uncertainty, represented by the magnitude of the deviation  $|\delta x_0|$ . The  $TEMoN_{\Phi}$  value based on the STT changes rapidly when LDT is high, but is cumulative, so is also dependent on the total time of propagation.

### 4.3 Orbit Results

A similar process was used to select thresholds for  $\text{TEMoN}_{\Phi}$ ,  $MD^*$ , and differential entropy to indicate when the uncertainty will become non-Gaussian. First, all the metrics were computed at the time of the PW trigger as shown in Fig. 4. The differential entropy values cover a wide range over many orders of magnitude. This is an indication that the differential entropy is not as reliable of an indicator of non-Gaussian uncertainty. The  $MD^*$  values show some interesting features for the L4 and L5 families, but  $MD^*$  remains in a tighter range over most orbits. The  $\text{TEMoN}_{\Phi}$  plot uses the same scale as the  $MD^*$  results for easier comparison, showing the tightest grouping of values. Thus, the  $\text{TEMoN}_{\Phi}$  metric is the most reliable and consistent indicator on non-Gaussian uncertainty. However, the  $MD^*$  metric may be a viable second choice for situations in which the propagation of STTs may be too difficult or computationally costly. The occurrence of peaks and variability in the metrics is probably due in part to an inexact determination of non-Gaussian uncertainty. It is also in part due to the PW trigger giving erratic results when there are multiple points in the orbit where the uncertainty gets close to being non-Gaussian.

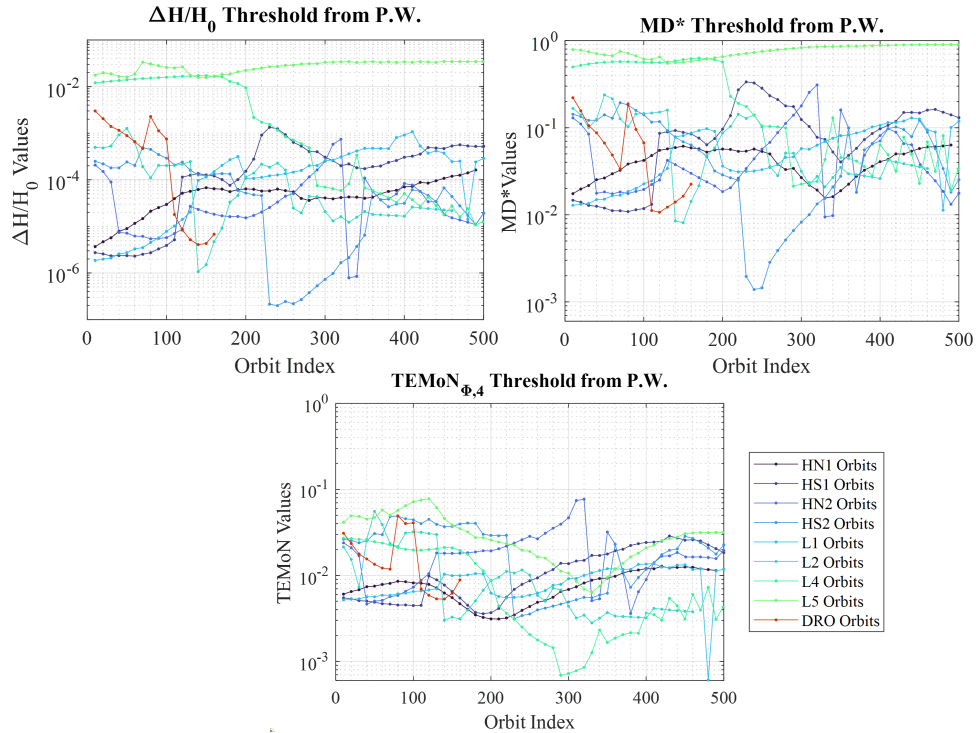


Fig. 4: Comparing the two Gaussian measures  $\Delta H/H_0$  and  $MD^*$  with  $\text{TEMoN}_{\Phi,4}$  obtained from PW for all orbits **H1**, **H2**, **L1**, **L2**, **L4**, **L5** and **DRO**.

Using the computed values for the TEMoN metric over all orbit indices, thresholds  $\varepsilon(PW)$  were selected for each orbit family by taking the 25th percentile value, denoted by  $\text{TEMoN}_{\Phi,4}^{\varepsilon}$ . The TEMoN threshold was used to predict the time the uncertainty became non-Gaussian. This is then compared to when the uncertainty became non-Gaussian according to the Monte Carlo-based  $PW$  metric. The bottom plots of Fig. 5, 6, 7, 8 and right plot of Fig. 9 compare the threshold times associated with  $PW$  and  $\text{TEMoN}_{\Phi,4}^{\varepsilon}$ . Such that the top plots superimpose the  $PW$  and  $\text{TEMoN}_{\Phi,4}^{\varepsilon}$  onto the TEMoN surface.

The plot for **H1** in Fig. 5 includes both northern and southern subdivisions of **H1**. The threshold times computed by  $\text{TEMoN}_{\Phi}^{\varepsilon}$  and  $PW$  differ by up to 5% of the orbit period time. For **H2** from Fig. 6 the TEMoN threshold times vary more for lower orbit indices. However, for higher orbit indices, a sharp peak in TEMoN occurs early in the trajectories and the TEMoN threshold is triggered consistently at nearly the same time as  $PW$ . It is shown that when there is a sudden increase in the non-linearity of the dynamics, it is easier to determine when the uncertainty becomes non-Gaussian. This apparent characteristic can be seen during a close approach to a primary body. The concept is reinforced in both **L1** and **L2** from Fig. 7 and **L4** and **L5** from Fig. 8.

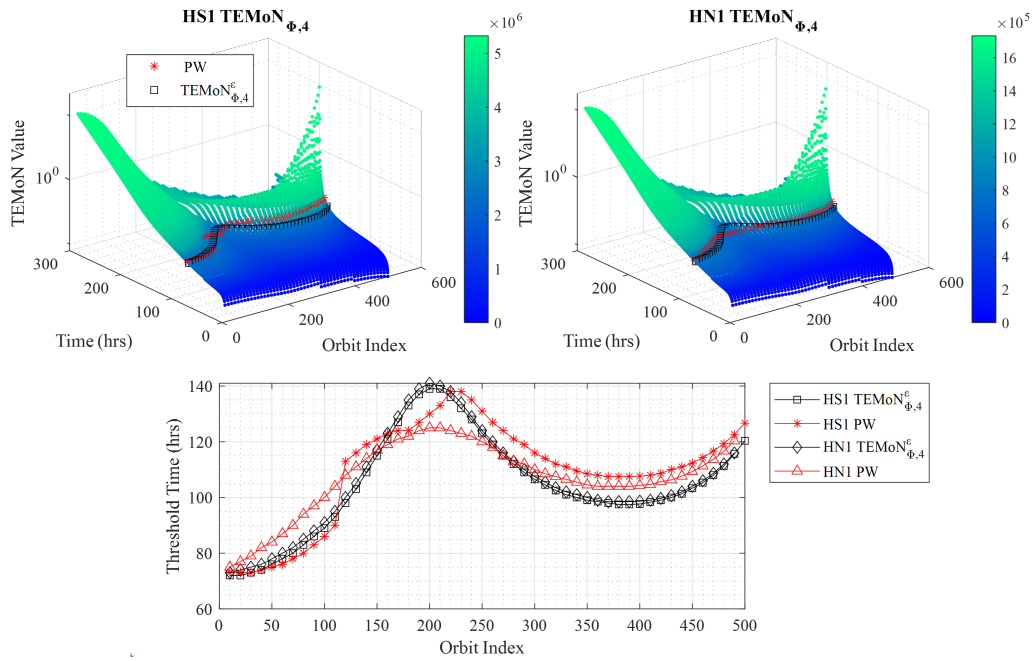


Fig. 5: Illustration of different threshold propagation times superimposed onto TEMoN surfaces for Halo from L1. Threshold times are selected from associated TEMoN $_{\Phi,4}$ (PW), and TEMoN $_{\Phi,4}^{\epsilon}$  thresholds occurred for Halo from L1. (left) Southern Halo from L1 TEMoN $_{\Phi,4}$ , (right) Northern Halo from L1 TEMoN $_{\Phi,4}$ . (bottom) Time thresholds compared on same scale.

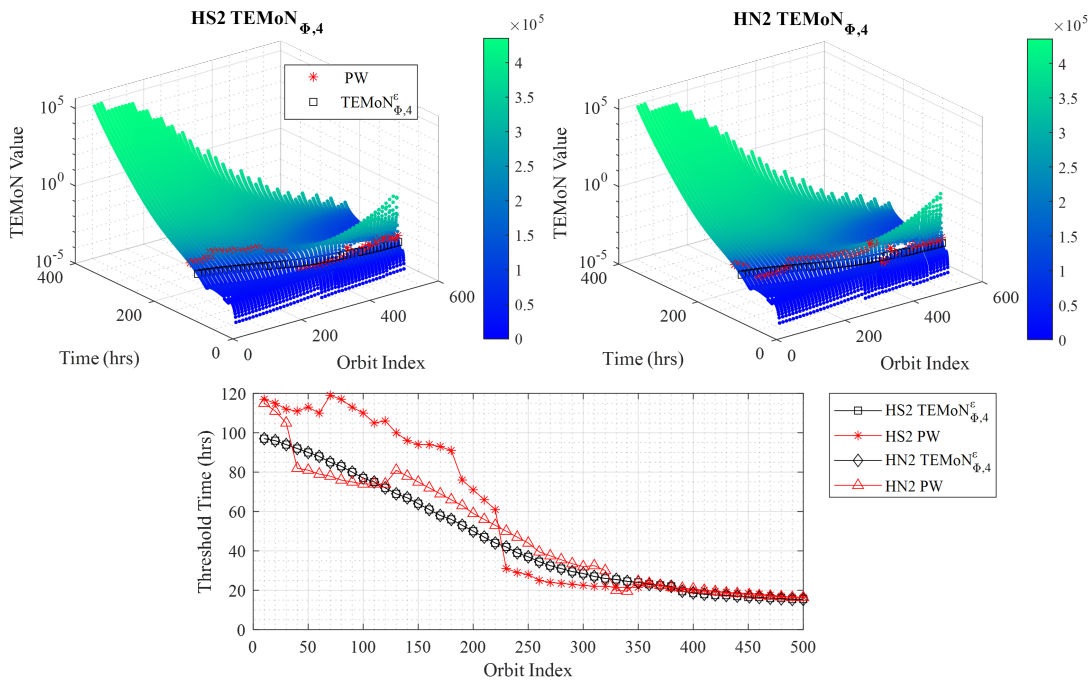


Fig. 6: Illustration of different threshold propagation times superimposed onto TEMoN surfaces for Halo from L2. (left) Southern Halo from L2 TEMoN $_{\Phi,4}$ , (right) Northern Halo from L2 TEMoN $_{\Phi,4}$ . (bottom) Time thresholds compared on same scale.

Approved for public release; distribution is unlimited. Public Affairs release approval #AFRL-2022-4065. The views expressed are those of the authors and do not reflect the official guidance or position of the United States Government, the Department of Defense or of the United States Air Force.

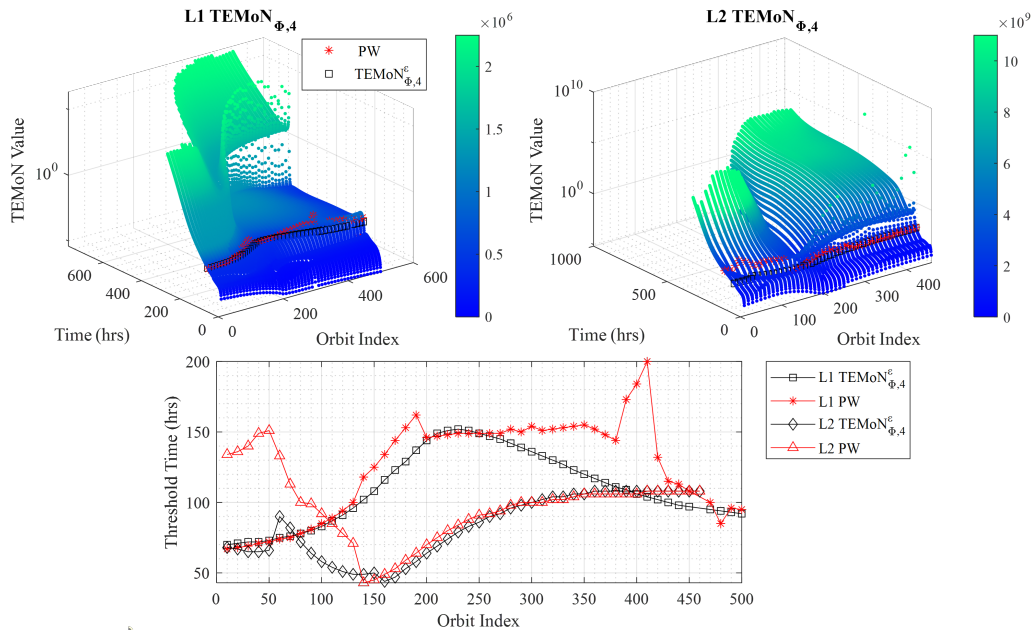


Fig. 7: Threshold time from initial point on orbit where  $TEMoN_{\Phi,4}$  threshold value occurred for orbit families Lyapunov from  $L_1$  and Lyapunov from  $L_2$ . (left) Lyapunov from  $L_1$   $TEMoN_{\Phi,4}$ , (right) Lyapunov from  $L_2$   $TEMoN_{\Phi,4}$ . (bottom) Time thresholds compared on same scale.

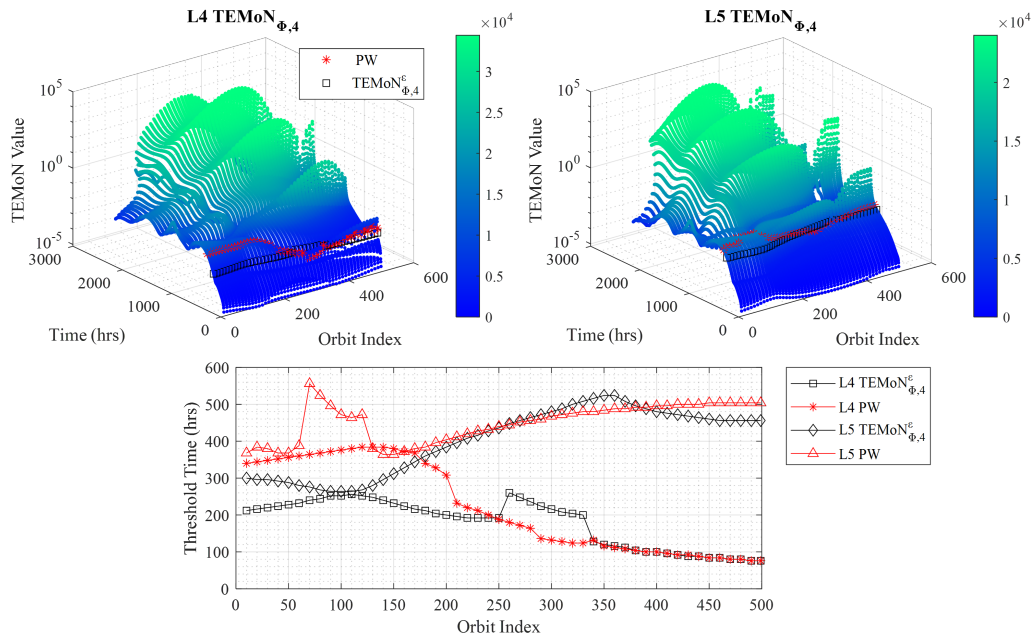


Fig. 8: Threshold time from initial point on orbit where  $TEMoN_{\Phi,4}$  threshold value occurred for orbit families Long-Period from  $L_4$  and Long-Period from  $L_5$ . (left) Long-Period from  $L_4$   $TEMoN_{\Phi,4}$ , (right) Long-Period from  $L_5$   $TEMoN_{\Phi,4}$ . (bottom) Time thresholds compared on same scale.

There is a periodic fluctuation of the  $L_4$  and  $L_5$   $TEMoN$  surfaces as shown in Fig. 8. It shows that, depending on which peak in non-linearity triggers the threshold, there can be large differences in trigger times. In contrast to  $L_4$  and

Approved for public release; distribution is unlimited. Public Affairs release approval #AFRL-2022-4065. The views expressed are those of the authors and do not reflect the official guidance or position of the United States Government, the Department of Defense or of the United States Air Force.

**L5**, the DRO orbit family produces a smooth TEMoN surface in the left plot of Fig. 9, but that creates an additional complication. Because the surface is more smooth and flat, the trigger time is more sensitive to the threshold value. In other words, the transition from Gaussian to non-Gaussian is much more gradual, so it is more difficult to say exactly when the transition takes place.

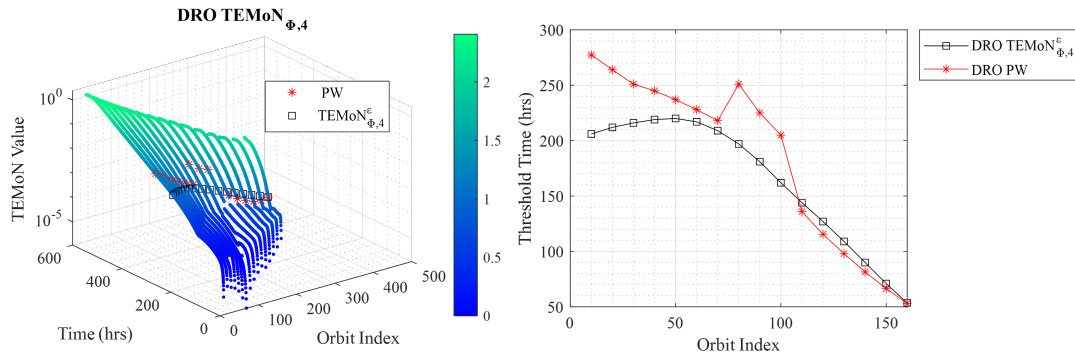


Fig. 9: Threshold time from initial point on orbit where  $\text{TEMoN}_{\Phi,4}$  threshold value occurred for DRO (left). Time thresholds compared on same scale (right).

## 5. SUMMARY AND FUTURE WORK

This paper explored how the degree of nonlinearity in the dynamics, as quantified by TEMoN, can be used to predict the transition from Gaussian to non-Gaussian uncertainty. The method is applied to the cislunar regime with a selection of orbit families defined as **H1**, **H2**, **L1**, **L2** and DRO. From Monte Carlo simulations with an optimized particle cloud representation of the initial Gaussian uncertainty, the PW metric is used to evaluate when the propagated uncertainty becomes non-Gaussian. Such that it is defined as the first time that less than 99.9% of the particles are within the probability ellipsoid propagated using sigma-points. The PW trigger is used to compute TEMoN values and those are used to select a TEMoN threshold to use as an indicator of non-Gaussian uncertainty. Additional Gaussian measures such as the evolutionary deviation of Mahalanobis distance and differential entropy were compared against TEMoN for the set of cislunar trajectories.

The depiction of a TEMoN surface composed of propagation time and TEMoN value over a set of orbits in a family demonstrates the importance in careful selection of TEMoN thresholds. Various features on the surface allude to the complex coupling of propagation time and non-linear effects. In addition, that it is difficult to quantify how ‘‘Gaussian’’ an uncertainty distribution is. This means that predicting the transition to non-Gaussian uncertainty will never be an exact science. However,  $MD^*$  and especially TEMoN do perform more reliably than the more customarily used differential entropy.

These metrics for indicating non-Gaussian uncertainty are relevant to current tasking methodologies, where sensors can be tasked to observe cislunar space objects preemptively in order to maintain the uncertainty as Gaussian. In some cases, especially with close lunar fly-bys, it may not be possible to keep the uncertainty from becoming non-Gaussian. Therefore, these metrics may be useful in triggering a method for switching to another representation of the uncertainty, such as Gaussian Mixture Models (GMM), Polynomial Chaos Expansion (PC), GMM-Unscented Transform, GMM-STTs and GMM-PC as described in [14].

This research can be expanded by trying non-periodic cislunar orbits and using different initial covariances. It can be further supplemented by investigating how the presence of other estimated parameters in the state affect results, and using of more comprehensive force models instead of the CRTBP.

## 6. REFERENCES

- [1] Kyle T Alfriend and Inkwan Park. When does the uncertainty become non-gaussian. In *Advanced Maui Optical and Space Surveillance Technologies Conference*, page 46, 2016.
- [2] Brett W Bader, Tamara G Kolda, et al. Tensor toolbox for matlab, version 2.2, 2008.
- [3] Douglas M Bates and Donald G Watts. Relative curvature measures of nonlinearity. *Journal of the Royal Statistical Society: Series B (Methodological)*, 42(1):1–16, 1980.
- [4] Meghan K Cain, Zhiyong Zhang, and Ke-Hai Yuan. Univariate and multivariate skewness and kurtosis for measuring nonnormality: Prevalence, influence and estimation. *Behavior research methods*, 49(5):1716–1735, 2017.
- [5] Cornelius Channing Chow II. *Autonomous interplanetary constellation design*. PhD thesis, 2012.
- [6] Kyle J DeMars, Robert H Bishop, and Moriba K Jah. Entropy-based approach for uncertainty propagation of nonlinear dynamical systems. *Journal of Guidance, Control, and Dynamics*, 36(4):1047–1057, 2013.
- [7] Kyle J DeMars, Robert H Bishop, and Moriba K Jan. A splitting gaussian mixture method for the propagation of uncertainty in orbital mechanics. *Spaceflight Mechanics*, 140, 2011.
- [8] Kyle Jordan DeMars. *Nonlinear orbit uncertainty prediction and rectification for space situational awareness*. PhD thesis, 2010.
- [9] Eusebius J Doedel, Volodymyr A Romanov, Randy C Paffenroth, Herbert B Keller, Donald J Dichmann, Jorge Galán-Vioque, and André Vanderbauwhede. Elemental periodic orbits associated with the libration points in the circular restricted 3-body problem. *International Journal of Bifurcation and Chaos*, 17(08):2625–2677, 2007.
- [10] Joshua T Horwood, Jeffrey M Aristoff, Navraj Singh, Aubrey B Poore, and Matthew D Hejduk. Beyond covariance realism: a new metric for uncertainty realism. In *Signal and Data Processing of Small Targets 2014*, volume 9092, page 90920F. International Society for Optics and Photonics, 2014.
- [11] Erica L Jenson and Daniel J Scheeres. Semianalytical measures of nonlinearity based on tensor eigenpairs. In *Proc. AAS/AIAA Astrodynamics Specialist Conference*, 2021.
- [12] Simon Julier, Jeffrey Uhlmann, and Hugh F Durrant-Whyte. A new method for the nonlinear transformation of means and covariances in filters and estimators. *IEEE Transactions on automatic control*, 45(3):477–482, 2000.
- [13] John L Junkins and Puneet Singla. How nonlinear is it? a tutorial on nonlinearity of orbit and attitude dynamics. *The Journal of the Astronautical Sciences*, 52(1):7–60, 2004.
- [14] Ya-zhong Luo and Zhen Yang. A review of uncertainty propagation in orbital mechanics. *Progress in Aerospace Sciences*, 89:23–39, 2017.
- [15] Carl D Murray and Stanley F Dermott. *Solar system dynamics*. Cambridge university press, 1999.
- [16] Ryan S Park and Daniel J Scheeres. Nonlinear mapping of gaussian statistics: theory and applications to spacecraft trajectory design. *Journal of guidance, Control, and Dynamics*, 29(6):1367–1375, 2006.
- [17] Claude Elwood Shannon. A mathematical theory of communication. *The Bell system technical journal*, 27(3):379–423, 1948.
- [18] Jason Stauch and Moriba Jah. Unscented schmidt–kalman filter algorithm. *Journal of Guidance, Control, and Dynamics*, 38(1):117–123, 2015.
- [19] Rudolph Van Der Merwe. *Sigma-point Kalman filters for probabilistic inference in dynamic state-space models*. Oregon Health & Science University, 2004.
- [20] Emily M Zimovan. Characteristics and design strategies for near rectilinear halo orbits within the earth-moon system. Master’s thesis, Purdue University, 2017.